Case Studies in Thermal Engineering 28 (2021) 101668

Contents lists available at ScienceDirect

Case Studies in Thermal Engineering

journal homepage: www.elsevier.com/locate/csite

Critical heat flux prediction model of pool boiling heat transfer on the micro-pillar surfaces

Yonghai Zhang [a,b], Xiang Ma [b,*], Zhiqiang Zhu [c,d,**], Lian Duan [b], Jinjia Wei [b,e]

[a] Shenzhen Research Institute, Xi'an Jiaotong University, Shenzhen, Guangdong, 518057, PR China
[b] School of Chemical Engineering and Technology, Xi'an Jiaotong University, Xi'an, Shanxi, 710049, PR China
[c] Key Laboratory of Microgravity, Institute of Mechanics, Chinese Academy of Sciences, Beijing, 100190, PR China
[d] School of Engineering Science, University of Chinese Academy of Sciences, Beijing, 100049, PR China
[e] Key Laboratory of Multiphase Flow in Power Engineering, Xi'an Jiaotong University, Xi'an, 710049, PR China

HIGHLIGHTS

- Experiments of pool boiling heat transfer on surfaces with micro-pillars were performed.
- The effects of the replenished liquid velocity, vapor column radius and vapor column spacing on the CHF were analyzed.
- A CHF predicted model for surfaces with micro-pillars was proposed.

ARTICLE INFO

Keywords:
Critical heat flux
Prediction model
Pool boiling
Micro-pillar surfaces

ABSTRACT

An pool boiling heat transfer experimental investigation was studied on the surfaces with micro-pillars using FC-72 as working fluid. The pool boiling experiment was conducted under the saturated and subcooled conditions ($\Delta T_{sub} = 25$ K). It can be found that the critical heat flux (CHF) of surfaces wtih micro-pillars is higher than that of smooth chip, and the surface area enhancement ratio and the arrangement of the micro-pillars have significant effects on the CHF. The replenished liquid velocity u_l is proposed to evaluate the wicking effect. A new prediction model is established to predict the CHF of surfaces with micro-pillars considering the effect of replenished liquid velocity u_l, vapor column radius r_v and vapor column spacing λ_b. The results show that the new CHF prediction model can effectively reflect the impact of the micro-pillars on CHF, and the experimental data can be predicted with an error band of ± 10%, indicating a good predicted ability.

1. Introduction

In recent years, pool boiling heat transfer has been widely studied and applied to many fields, such as micro-computers, communications, batteries and aerospace thermal management. Boiling heat transfer with the latent heat of working fluid has higher heat efficiency than that of single-phase heat transfer. However, with the rapid development of the micro-miniaturization equipment, more heat from the electronic devices needs to be dissipated. Micro-structured surface was considered as an effective method to enhance pool boiling heat transfer performance in recent literature [1–9].

Wei and Honda [1] fabricated square micro-pin-fins on the silicon chip by using microelectronic fabrication techniques. Xun et al. [2,3] investigated the effect of interfacial heat transfer on thermocapillary flow in a cylindrical liquid bridge. The interfacial heat

* Corresponding author.
** Corresponding author. Key Laboratory of Microgravity, Institute of Mechanics, Chinese Academy of Sciences, Beijing, 100190, PR China.
E-mail addresses: maxiang7632@stu.xjtu.edu.cn (X. Ma), zhuzhiqiang@imech.ac.cn (Z. Zhu).

https://doi.org/10.1016/j.csite.2021.101668
Received 11 October 2021; Received in revised form 11 November 2021; Accepted 20 November 2021

Available online 22 November 2021
2214-157X/© 2021 The Authors. Published by Elsevier Ltd. This is an open access article under the CC BY-NC-ND license (http://creativecommons.org/licenses/by-nc-nd/4.0/).

transfer can modify the free-surface temperature distribution and then induce a steeper temperature gradient. Additionally, the interfacial heat transfer restrains the temperature disturbance and stabilizes the convection. Dong et al. [5] prepared four structures on the tested samples. The surfaces with micro-pillars and micro-cavities were fabricated by dry etching process while the surfaces with nanowires and nano-cavities were immersed into the etching solutions containing $AgNO_3$ and hydrofluoric acid. Cao et al. [8] fabricated two kinds of micro-pin-fins on silicon surfaces, which were further modified by depositing FeMn oxide nanoparticles (~35 nm). Jo et al. [10] used photoresist lithograph and dry etching methods to fabricate micro-post structures with the contact angle of < 90° on the test section. The micro-post diameter, height and pitch were 110, 20 and 130 μm, respectively. Kim et al. [11] prepared a bare surface and four micro-structured surfaces with microscale gaps ranging from 5 to 80 μm. And the effects of micro-structured surface on bubble growth and dynamics were examined and analyzed using a simple model. Liu et al. [12,13] investigated the pool boiling CHF mechanism on the femtosecond laser processed surfaces with different processing spacing and height. They found that the CHF has a remarkable improvement on the femtosecond laser processed surfaces with higher processing height compared with that of smooth surface. Zhang et al. [14] also thought that the fin pitch and configuration have an significant effect on the pool boiling heat transfer characteristics.

Many researchers have demonstrated the micro-structured surfaces have a positive effect on increasing CHF and reducing the wall superheat. And the liquid subcooling and wickability distribution of the microstructures also play an important role in analyzing the CHF mechanism. Lei et al. [7] investigated the pool boiling heat transfer performance using surfaces with six kinds of the radical micro-pillars under different liquid subcoolings (0 K, 15 K, 25 K, 35 K). They found that the block divisions and blank area could effectively prevent vapor columns from coalescing. Kong et al. [15] found a micronization boiling phenomenon on the bistructured surfaces, which can produce more nucleation sites and enhance the heat transfer performance in the nucleate boiling heat transfer region. Zhou et al. [16] analyzed the effects of distribution and liquid subcooling on the CHF. The results indicated the CHF of fractal surfaces increases first and then decreases with the increase of fractal dimension under the different liquid subcoolings. The liquid replenishment on the micro-structured surfaces could delay the wall dryout and achieve higher CHF. And the liquid subcooling has been also proved to promote the liquid supply by affecting the bubble size in **Refs.** [6,7,17].

While coating surfaces with enhanced wetting properties, wickability and nucleation sites have been proved to improve the CHF and heat transfer coefficient (HTC). Capillary wicking tests were performed to explore the pool boiling heat transfer characteristics using deionized water on a zirconium surface in **Ref.** [4], the amount of water absorption indicates the effective capillary wicking on the surface and explains the CHF enhancement mechanism of the zirconium surface. Rahman et al. [18] reported that the super-hydrophilic surface achieves a CHF of 257 W/cm^2 using deionized water. Chu et al. [19] investigated the effect of the surface roughness-augmented wettability on CHF during pool boiling. They thought that the roughness-amplified capillary force is the reasons for the CHF enhancement on micro-structured surfaces.

CHF in pool boiling is a vital significant parameter which can avoid damaging devices. So it has great importance for operators to control the wall superheat and predict the CHF of pool boiling for various micro-structured surfaces. A theoretical model is of vital significance to study the CHF mechanism. During the past decades, several theoretical models were proposed for predicting the pool boiling CHF. In 1958, Zuber [20] proposed an CHF calculation method on a infinite horizontal smooth surface based on vapor-liquid hydrodynamics unstable model for saturated pool boiling. Then Liter and Kaviany [21] proposed several different CHF prediction models on several coating surfaces, including deep porous-layer coating, uniform and thin porous-layer coating and moudulated porous-layer coating. In 2001, Kanklikar [22] described the bubble behaviors on the heated surface. A theoretical model was developed by considering the effects of the dynamic contact angle and liquid subcoolings. And this model can also predict the experimental data well for different fluid, including water, refrigerants and cryogenic liquid, which is valid for orientations from 0 deg (horizontal surface) to 90 deg (vertical surface). Based on the pool boiling CHF model of Kandlikar [22], Quan et al. [23] presented a theoretical model to predict the CHF for saturated pool boiling on a heated surface with micro/nano-structures based on a force balance analysis considering the effects of the capillary wicking force and modifying the critical instability wavelength. Dhillon et al. [24] found the dynamics of dry spot heating and rewetting phenomenon on the nano-textured micro-pillar surface. They thought the

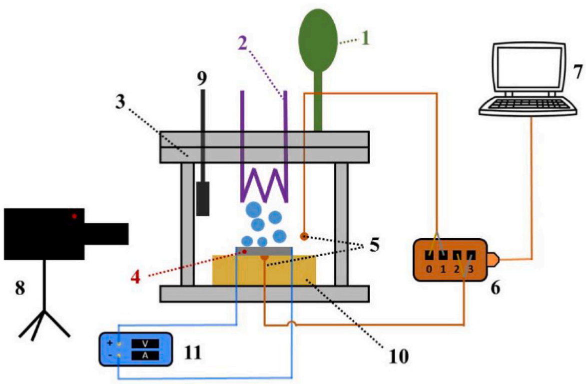

Fig. 1. Schematic diagram of experimental setup: 1. Rugger bag, 2. Condenser, 3. Boiling chamber, 4. Test chip, 5. Thermocouples, 6. Data acquisition, 7. Computer, 8. High-speed camera, 9. Heating rod, 10. Pedestal, 11. DC power supply.

dry spot heating timescale is of the same order as that of the gravity and liquid imnition-induced dry spot rewetting timescale. A coupled thermal-hydraulic model related CHF enhancement to rewetting phenomenon of a hot dry spot on the boiling surface was proposed. Wu et al. [25] developed a newly model to predict the boiling curve of modified surfaces by considering the heat flux contributions from microlayer evaporation, transient heat conduction and micro-convection. Furthermore, Ahn et al. [4], Cao et al. [8], Guan et al. [9], Zhang et al. [14] and Zhou et al. [17] have also modified the traditional theoretical model to predict the pool boiling CHF accounting for the effect of the microstructures, wickability and liquid subcooling.

It can be found from the above introduction that the distribution of microstructures and capillary wickability have an important influence on the CHF enhancement mechanism. But there are few studies focusing on the non-uniformity of microstructures. In this study, an pool boiling experiment has been conducted on the surfaces with uniform and non-uniform micro-pillars. And a new idea was proposed to predict CHF of surfaces with micro-pillars by considering the non-uniformity and surface area enhancement ratio.

2. Experimental methods

2.1. Experimental setup

Fig. 1 shows a schematic diagram of the experimental apparatus. The experimental setup is composed of a boiling chamber, a tested silicon chip, a data acquisition system, a rugger bag, a condenser, a heat rod, a DC power supply and a high-speed camera. The boiling chamber is made of PMMA, which is filled with FC-72 ($T_{sat} = 329$ K at 1atm). A rugger bag is used to maintain the pressure of the boiling chamber at 1atm. The tested silicon chip with a side length of 10 mm and a thickness of 0.5 mm is placed on the pedestal, which is heated by the DC power supply. The temperature of the wall and the fluid are measured by T-type thermocouples with a calibrated accuracy of 0.4 K. The liquid temperature can be adjusted by the heating rod and condenser. The pool boiling heat transfer characteristics are investigated under saturated and subcooled conditions ($\Delta T_{sub} = 25$ K), respectively. In order to achieve stable experimental conditions, the data points were collected over 20 s (average 20 points, each with internal of 1 s) with deviations of temperature below 0.4 K. A high-speed camera is used to record the bubble behaviors. Additional details of the experimental apparatus and procedure can be obtained in the literature [6].

2.2. Surface structures characteristics

In this study, a dry etching method is used to fabricate the micro-pillars on the silicon chip. The five samples are named as U–S, U-M, U-L, R-SML and R-SL based on the size of micro-pillars. These surfaces with micro-pillars are composed by three categories pillars with the diameter of 25 μm (S-type), 50 μm (M-type) and 100 μm (L-type), respectively. The height of three kinds of micro-pillars is 120 μm. The scanning electron microscope (SEM) images of these surfaces are shown in Fig. 2. The geometry parameters of all surfaces are presented in Table 1.

U– S, U-M and U-L are three surfaces with uniform micro-pillars, and the center distance of micro-pillars are 50 μm, 100 μm and 200 μm, respectively. For R-SML and R-SL surfaces, the size of micro-pillars is different. As shown in Fig. 2(d)–(e), the distribution of micro-pillars is non-uniform, R-SML is composed of three kinds of micro-pillars (S-type, M-type and L-type), and the R-SM is composed by two kinds of micro-pillars (S-type and M-type). The parameters N_S, N_M and N_L are the number of S-type, M-type and L-type micro-pillars for five surfaces, which have been listed in Table 1. The α is the surface area enhancement ratio, which is defined as the ratio of the actual heat transfer area of micro-structured surface to that of smooth surface.

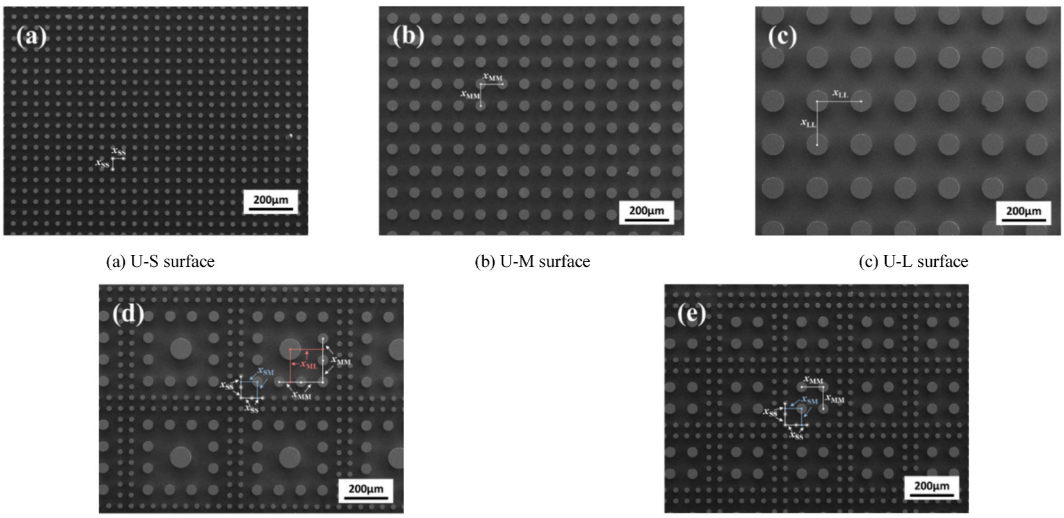

(a) U-S surface (b) U-M surface (c) U-L surface

(d) R-SML surface (e) R-SM surface

Fig. 2. SEM images of micro-pillar surfaces before experiment (a) U–S, (b) U-M, (c) U-L, (d) R-SML, (e) R-SM.

Table 1
Geometry parameters of these tested micro-pillar surfaces.

Sample	x_{SS}	x_{SM}	x_{MM}	x_{ML}	x_{LL}	N_S	N_M	N_L	α
U–S	50	–	–	–	–	39,601	–	–	4.73
U-M	–	–	100	–	–	–	10,000	–	2.88
U-L	–	–	–	–	200	–	–	2,500	1.94
R-SML	50	75	100	150	200	14,400	4,800	400	3.41
R-SM	50	75	100	–	–	21,780	4,356	–	3.87

2.3. Uncertain analysis

The heat flux can be calculated by the voltage U and current I supplied by the DC power:

$$q = \frac{U \cdot I}{A} \tag{1}$$

where A is the heat transfer area of the test chip ($A = L \times L$). In this research, the measurement uncertainties in U, I and L are 0.1%, 0.45% and 0.5%, respectively. Uncertainty of the dependent quantities can be calculated using the follow equations based on error delivering theory. So the uncertainty of the heat flux can be calculated as follow:

$$\xi(q) = \sqrt{\left(\frac{\partial^2 U}{U^2}\right) + \left(\frac{\partial^2 I}{I^2}\right) + 4\left(\frac{\partial^2 L}{L^2}\right)} \tag{2}$$

In addition, since the temperature difference of the bottom wall and the fluid is smaller than the fluctuations of the temperature (0.4 K), so it can be neglected and the bottom temperature of the test chip is approximately equal to the boiling surface temperature. And the heat loss by conduction through test chip, cooper wires and substrate should be taken into consideration, which is approximately 5%. Therefore, it can be found that the uncertainty in the determination of total heat flux was within 7% for all the test runs. Experimental uncertainties for all measured parameters are summarized in Table 2.

2.4. Boiling curve

Fig. 3 shows the boiling curve under the saturated and subcooled conditions ($\Delta T_{sub} = 25$ K), including smooth, uniform and non-uniform micro-pillar surfaces. The superheat temperature and CHF of the different surfaces are shown in Table 3. The smooth surface has the smallest CHF value among all the tested samples.

For the surfaces with uniform micro-pillars, the CHF values has little difference at saturated boiling as shown in Fig. 3(a). The CHF values are approximately 1.7–1.8 times higher than that of smooth surface. So it can be thought that the size of micro-pillars has little influence on increasing the saturated pool boiling CHF. But the superheat temperature at critical status increases with the diameter and spacing of micro-pillars increasing. The U–S surface can keep lower wall temperature at the same heat flux. It can be contributed to the higher surface area enhancement ratio ($\alpha_{U\text{-}S} = 4.73$). Under the subcooled pool boiling, it can be also found that the three surfaces with uniform micro-pillars show higher CHF values and lower wall temperature compared with the smooth surface. And the liquid subcooling has a positive effect on increasing the CHF. However, for the surfaces with non-uniform micro-pillars, the CHF has an obvious increase especially at the subcooled pool boiling ($\Delta T_{sub} = 25$K) as shown in Fig. 3(d).

In order to further analyze the reason of the higher CHF on the surfaces with non-uniform micro-pillars, the next section will analyze the pool boiling heat transfer mechanism and propose a new model to predict the CHF considering the liquid supply capacity and vapor column for the surfaces with micro-pillars, and the CHF enhancement mechanism on the non-uniform micro-pillars is also discussed in depth.

3. CHF model

3.1. Basic preparation and assumptions

Based on the instability of the vapor column and the replenished liquid on the surfaces with micro-pillars, we established a model to predict the pool boiling CHF. The entire computational process is shown in **Fig. 4**.

The method raised up in this study introduced two hypothesis:

Table 2
Uncertainties of the measurements.

Parameters	Uncertainty
Length of the test chip L, (mm)	0.5%
Voltage U, (V)	0.15%
Current I, (A)	0.45%
Heat loss q_{loss}, (W/cm^2)	5%
Heat flux q, (W/cm^2)	6.6%

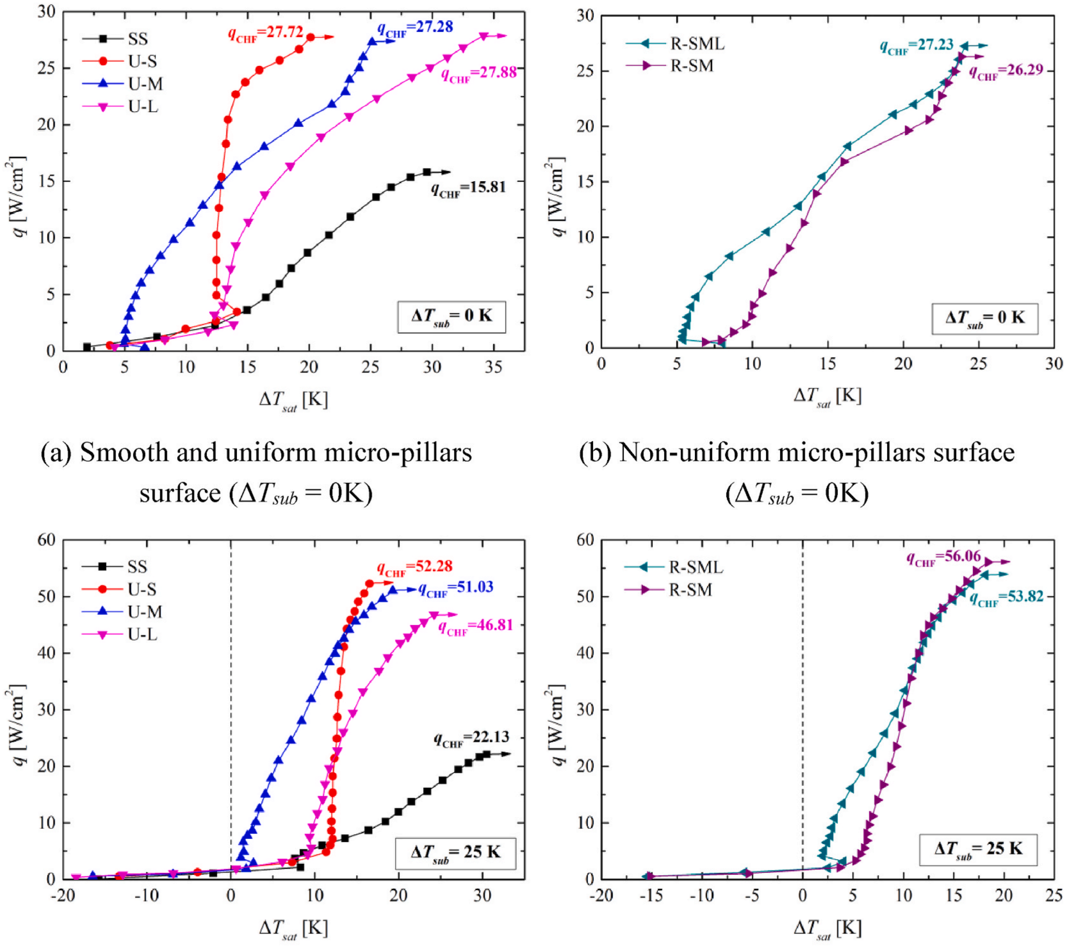

(a) Smooth and uniform micro-pillars surface (ΔT_{sub} = 0K)

(b) Non-uniform micro-pillars surface (ΔT_{sub} = 0K)

(c) Smooth and uniform micro-pillars surface (ΔT_{sub} = 25K)

(d) Non-uniform micro-pillars surface (ΔT_{sub} = 25K)

Fig. 3. Boiling curves of uniform and non-uniform micro-pillars surfaces under saturated and subcooling boiling.

Table 3
Surface area enhancement ratio and CHF of the different micro-pillars surfaces.

Sample	Saturated (ΔT_{sub} = 0 K)		Subcooled (ΔT_{sub} = 25 K)	
	ΔT_{sat} (K)	CHF (W/cm^2)	ΔT_{sat} (K)	CHF (W/cm^2)
SS	29.56	15.81	30.49	22.13
U–S	20.11	27.72	16.54	52.28
U-M	25.11	27.28	19.28	51.03
U-L	34.17	27.88	24.21	46.81
R-SML	24.12	27.23	18.14	53.82
R-SM	23.83	26.29	18.38	56.06

3.1.1. *Same correction factor k for the different surfaces*

To calculate CHF, the replenished liquid velocity u_l on the surface is of vital significance. In this study, we assumed an ideal state that the pressure drop caused by the viscous resistance and capillary force are equal, and the influence of phase change and vapor disturbance during the pool boiling is neglected. Consider these reasons, the replenished liquid velocity u_l will be larger than the actual value, which needs to be corrected based on the experimental data. Therefore, the theoretical and experimental values of the replenished liquid velocity u_l on the U-M surface are used to calculate the correction factor k, which will be applied to other surfaces with micro-pillars.

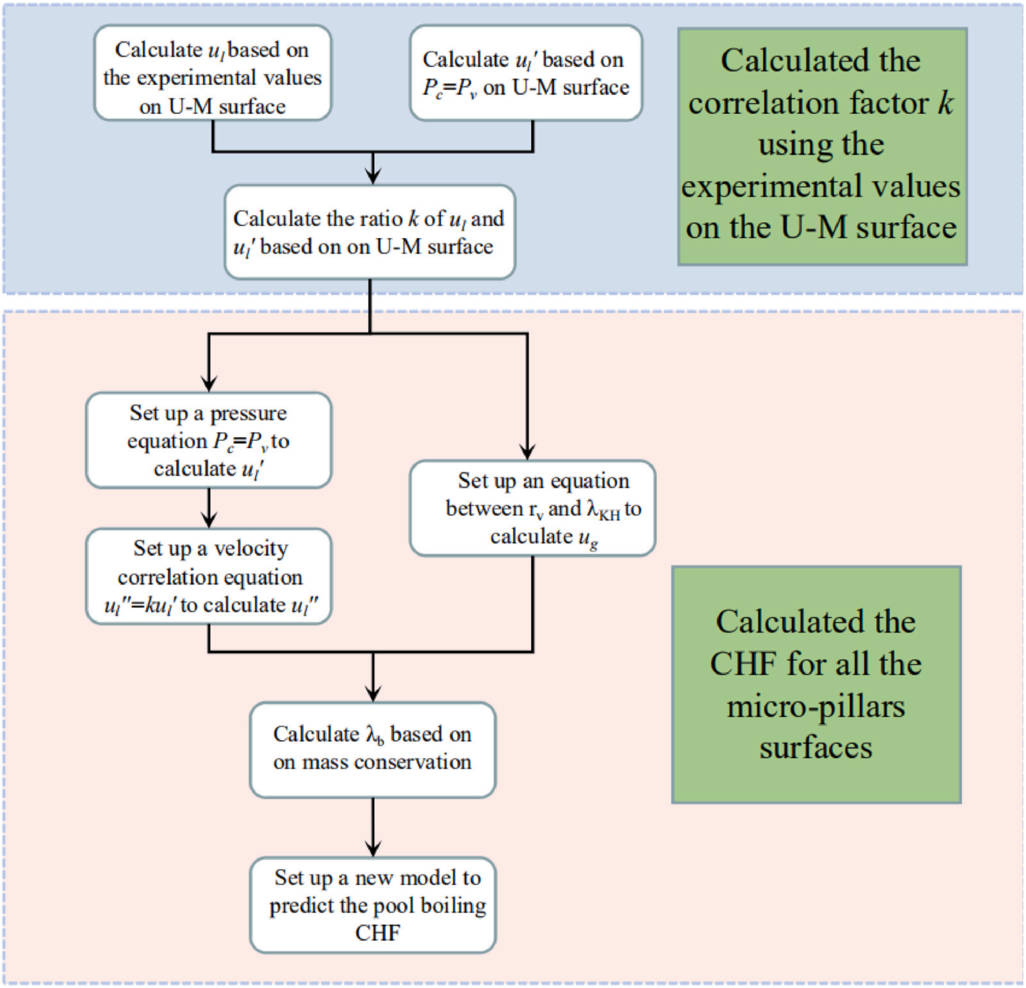

Fig. 4. Solution process for CHF prediction model.

3.1.2. All surfaces with micro-pillars have the same critical vapor column radius, which can be calculated by the Zuber's model [20]

Since the purpose of this new model is to predict pool boiling CHF of the surfaces with micro-pillars, the radius of the vapor column r_v in the computational process is the critical vapor column radius $r_{v,c}$. However, it has been already generally understood that the Zuber's model [20] is different from the actual phenomenon, in the high heat flux region including the CHF, the large coalesced bubbles cover the heated surface, and the macrolayer exists near the surface, etc. And the Zuber's model [20] is based on the smooth surface, the experimental values of the critical vapor column radius $r_{v,c}$ on the surfaces with micro-pillars are different from the predicted values by the Zuber's model [20]. In order to simplify the analysis and predict CHF conveniently, it is assumed that all micro-pillar and smooth surfaces have the same critical vapor column radius $r_{v,c}$. In addition, it is necessary to correct the vapor column radius under the subcooled condition, which will be described in Section 3.2.

3.2. Zuber's theoretical model

So far, Zuber's theoretical model [20,25] has been widely used for predicting the pool boiling CHF. As shown in Fig. 5, the gray, gold, light blue and red dashed line area are the silicon surface, the vapor column, the working fluid and the unit area, respectively. Zuber [20] thought that the vapor column was uniform distribution on the heated surface near the CHF as shown in Fig. 5(a). Select the red dashed line area as one unit to discuss, the each unit area is composed of a vapor column and surrounding replenished liquid. The CHF can be calculated as follow:

$$q_{CHF} = \frac{\rho_v u_v h_{lv} A_v}{A_b} \tag{3}$$

where ρ_v, u_v, h_{lv}, A_v and A_b are the vapor density, the vapor velocity, the latent heat of vaporization, the vapor column area and the unit area, respectively.

In Zuber's model [20], the spacing and radius of vapor column (λ_b and r_v) can be calculated by the following equations:

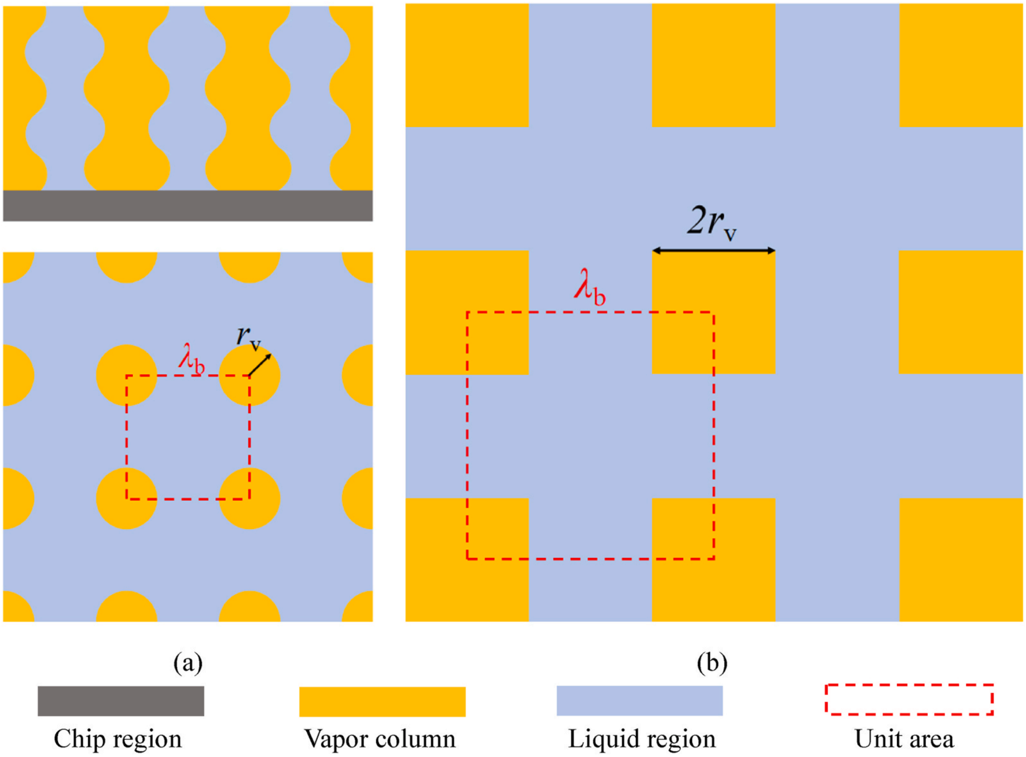

Fig. 5. The distribution schematic diagram of vapor columns (a) Zuber's model, (b) New model.

$$\lambda_b = \frac{9}{20}\lambda_{RT} \tag{4}$$

$$r_v = \frac{1}{2\pi}\lambda_{KH} \tag{5}$$

where λ_{RT} and λ_{KH} are the Rayleigh-Taylor instability wavelength and Kelvin-Helmholtz instability wavelength, which can be obtained by Eqs. (4)-(5), respectively.

$$\lambda_{RT} = 2\pi\sqrt{\frac{\sigma}{g(\rho_l - \rho_v)}} \tag{6}$$

$$\lambda_{KH} = \frac{2\pi\sigma}{\rho_v u_v^2} \tag{7}$$

Besides, in the Zuber's theoretical model hypothesis, the largest vapor column radius can be shown as follow:

$$r_v = \frac{1}{4}\lambda_b \tag{8}$$

Based on the above discussion, the Zuber's model [20] can be written as the follow equation:

$$q_{CHF} = \frac{\pi}{24}\rho_v^{0.5} h_{lv}[\sigma g(\rho_l - \rho_v)]^{0.25} \tag{9}$$

3.3. A new pool boiling CHF prediction model establishment and analysis

As shown in Fig. 5(b), we assumed that the vapor column is uniform distributed on the surfaces when it approached the CHF. Since the silicon and each unit area are square, it is assumed that the cross section of the vapor column is a square with a side length of $2r_v$, the vapor column spacing is λ_b, and the unit area is λ_b^2. The vapor column radius r_v can be obtained by Eqs. (4)–(8). It is remarkable that the empirical equation of the vapor column radius r_v in the Zuber's model is only valid under the saturated boiling, so it could not be applied to subcooled pool boiling. In the case of saturated boiling, the vapor column radius r_v is 1.608 mm.

At the $\Delta T_{sub} = 25$ K, since the size of vapor column is smaller than that of saturated boiling, Chen and Mayinger's model [26] is used to calculated the vapor column radius r_v instead of Zuber's model [20]. The radius of vapor column under the subcooled pool boiling is corrected as follows:

$$r_{v,sub} = \beta r_{v,sat} \tag{10}$$

$$\beta = \left(1 - 0.56\mathrm{Re}^{0.7}\mathrm{Pr}^{1/3} Ja \cdot Fo\right)^{0.9} \tag{11}$$

where $r_{v,sub}$ and $r_{v,sat}$ are the vapor column radius under the subcooled and saturated conditions, respectively, and β is the correction factor of the vapor column which is defined as the ratio of bubble radius at t moment to the initial bubble radius. Zhou et al. [17] obtained a correction factor of the vapor column ($\beta_{25\mathrm{K}} = 0.7$) by the experiments under the $\Delta T_{sub} = 25$ K, so the radius of vapor column at subcooled pool boiling ($\Delta T_{sub} = 25$ K) is 1.126 mm.

3.3.1. Solve the correction factor k

The capillary effect of the micro-pillars promotes the liquid replenishment resulting in the decrease of the vapor column and Rayleigh-Taylor instability wavelength. However, there is a liquid microlayer on the heated surface whose thickness is larger than the height of the micro-pillars, and the micro-pillars are covered by vapor columns. According to the mass conservation, the vapor velocity is much larger than the liquid replenishment velocity, which the vapor quality is equal to the replenished liquid in every vapor column unit time. Therefore, we assume that the influence of the micro-pillars on the Kelvin-Helmholtz instability wavelength is neglected, and the radius of the vapor columns and vapor velocity are approximately unchanged for different surfaces with micro-pillars.

$$r_v = \frac{\sigma}{\rho_v u_v^2} \tag{12}$$

$$\rho_v u_v \cdot 4r_v^2 = \rho_l u_l \cdot \left(\lambda_b^2 - 4r_v^2\right) \tag{13}$$

where u_l is the actual replenished liquid velocity.

The capillary force caused by the micro-pillars propels the liquid to flow to the vapor column area, which rewets the dryout area. The experimental CHF value on the U-M surface can be written as the follow equation by using Eq. (3):

$$\mathrm{CHF}_{\mathrm{U-M}} = \frac{\rho_v u_v \cdot 4r_v^2 h_{lv}}{\lambda_b^2} \tag{14}$$

Combined Eqs. 12–14, the actual velocity of the replenished liquid on the U-M surface under the saturated and subcooled pool boiling ($\Delta T_{sub} = 25$K) can be calculated as $u_{l,sat} = 3.969 \times 10^{-3}$ m/s and $u_{l,sub} = 7.839 \times 10^{-3}$ m/s. Therefore, the Reynolds number

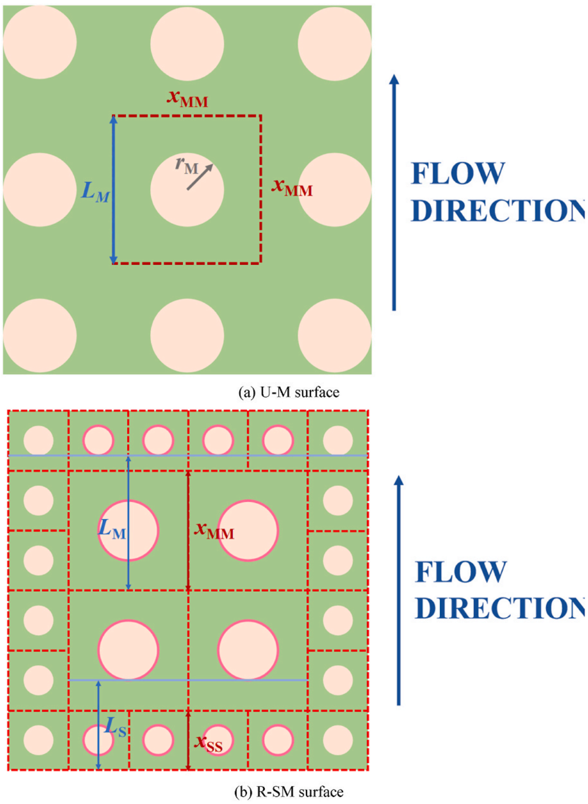

Fig. 6. The schematic diagram of the replenished liquid on the (a) U-M surface and (b) R-SM surface.

with the diameter of the pillars on the U-M surface as the characteristic length can be calculated as $\mathrm{Re}_{sat} = 0.718$ and $\mathrm{Re}_{sub} = 1.097$.

The effect of the micro-pillars on the boiling heat transfer is governed by a balance between the capillary pressure (P_c) and the viscous pressure drop (P_v) associated with the liquid flow in the micro-pillars. Therefore, theoretical replenished liquid velocity u_l' can be calculated based on the model theory proposed by Dhillon et al. [24], which the capillary pressure P_c is equal to the viscous resistance pressure P_v.

Capillary pressure drop ΔP_c is the ratio between the system energy change ΔE and the liquid volume ΔV.

$$P_c = -\frac{\Delta E}{\Delta V} \tag{15}$$

Fig. 6(a) presents the calculation process of the capillary pressure taking U-M surface as an example. The unit volume ΔV is occupied by the liquid entering a certain vapor column, which can be expressed as:

$$\Delta V = \left(x_{MM}^2 - \pi r_M^2\right) h_o \tag{16}$$

where h_o is the height of the micro-pillars (120 μm). The energy change ΔE is composed of ΔE_1, ΔE_2 and ΔE_3, which represents the loss energy at the solid-vapor interface, the newly generated energy at the solid-liquid and vapor-liquid interface, respectively. These energy changes can be calculated as follow equations:

$$\Delta E = \Delta E_1 + \Delta E_2 + \Delta E_3 \tag{17}$$

$$\Delta E_1 = -\left(x_{MM}^2 - \pi r_M^2 + 2\pi r_M h_0\right)\sigma_{sv} \tag{18}$$

$$\Delta E_2 = \left(x_{MM}^2 - \pi r_M^2 + 2\pi r_M h_0\right)\sigma_{sl} \tag{19}$$

$$\Delta E_3 = \left(x_{MM}^2 - \pi r_M^2\right)\sigma_{lv} \tag{20}$$

where σ_{sv}, σ_{sl} and σ_{lv} are the surface tension at the solid-vapor, solid-liquid and liquid-vapor interface, respectively. And these energy changes can be considered as the increase (or loss) of the interface area multiplied by the surface tension.

The force equilibrium at the triple point can be expressed based on the Young's model [27]:

$$\sigma_{sv} - \sigma_{sl} = \sigma_{lv}\cos\theta \tag{21}$$

where θ is the contact angle of FC-72 on the smooth surface.

So the capillary pressure P_c on the U-M surface under the saturated and subcooled pool boiling can be calculated as $P_{c,sat} = 154.41$ Pa and $P_{c,sub} = 196.24$ Pa, respectively. The viscous resistance pressure P_v can be expressed as follow:

$$P_v = \frac{\mu u_l' r_v}{K_v} \tag{22}$$

where μ is the dynamic viscous of the liquid, K_v is the permeability of the surfaces with micro-pillars which is defined as follow:

$$K_v = \frac{\mu u_l'}{\Delta P} = \frac{\mu u_l'}{\Delta P_1 + \Delta P_2} \tag{23}$$

And ΔP represents the pressure drop per unit length of the replenished liquid flowing along the flow direction. Theoretically, it can be obtained by solving the Navier-Stokes equation. A simplified process is used due to the complicated theoretical solution: the liquid flow on the surfaces with micro-pillars consists of the flow along an infinite plate and the flow around an infinite pillar.

When the liquid flow along an infinite plate, it can be regarded that the thickness of the liquid is the height of the micro-pillars h_0. There is no velocity slippage phenomenon at the position where it is in contact with the surface, and the shear stress on the top of the liquid is zero. The pressure gradient of the liquid along the flow direction of an infinite plate can be obtained by incorporating the above two boundary conditions into the Navier-Stokes equation.

$$\Delta P_1 = \frac{3\mu u_l'}{h_0^2} \tag{24}$$

For the flow around an infinite pillar, the resistance of the pillar F_D consists of pressure drop resistance and viscous resistance. And it is a function of the Reynolds number with the pillar diameter D as the characteristic length, which can be calculated as:

$$F_D = \frac{1}{2} f_D \rho_l u_l' 2S = f(\mathrm{Re}_D) \tag{25}$$

where S is the facing flow area of the pillar, which is equal to the diameter of the pillar D in two dimensions. f_D is the resistance factor, and it presents an approximate inverse correlation with the Reynolds number Re_D. According to the Reynolds number under the different experimental conditions, the resistance factor can be calculated as $f_{D,sat} \approx 12$, $f_{D,sub} \approx 10$ [28]. So the pressure drop gradient of the flow around an infinite pillar can be derived as follow:

$$\Delta P_2 = \mathrm{Re}_D \frac{f_D \mu u_l'}{2 L_M x_{MM}} \tag{26}$$

where L_M is the length of the each unit area in the flow direction of replenished liquid as shown in Fig. 6(a). For the uniform micro-pillars, the length L_M is equal to the spacing of the micro-pillars x_{MM}, so the resistance affected area is limited to each micro-pillar unit. Eq. (26) can be further written as:

$$\Delta P_2 = \mathrm{Re}_D \frac{f_D \mu u_l'}{2 x_{MM}^2} \tag{27}$$

The sum of two part pressure drop gradient (ΔP_1 and ΔP_2) is the total pressure drop gradient ΔP of the surface replenished liquid. The viscous resistance pressure drop can be calculated by using Eqs. 22 and 23, which is a function of the replenished liquid velocity u_l'. So the capillary force pressure P_c and viscous resistance pressure P_v can be further expressed as following Eq. (28). At the same time, the replenished liquid velocity u_l' can be also obtained.

$$P_c = P_v(u_l') = \frac{\mu u_l' r_v}{K_v} \tag{28}$$

A correction factor k can be obtained by the ratio of actual replenished liquid velocity u_l to the theoretical replenished liquid velocity u_l', which are calculated as $k_{sat} = 0.0123$, $k_{sub} = 0.0216$.

$$k = \frac{u_l}{u_l'} \tag{29}$$

The correction factor k is only used to correct the liquid replenishment velocity u_l, which indicates the difference between the experimental values and the theoretical calculation values. The reason is that the boiling effect is not considered in the theoretical replenished liquid velocity u_l', which is only a theoretical velocity of liquid movement from the balance between the capillary pressure and viscous resistance of the micro-pillars. During the pool boiling, the heating surface is completely covered by the liquid, and the disturbance of bubbles is significant obviously. Therefore, the actual liquid replenishment velocity u_l on the micro-pillar surfaces is completely different from the boiling progress and need to be modified.

3.3.2. Set up a new CHF prediction model

As illustrated above, the process of calculating the pressure drop gradient on the U–S and U-L surfaces is similar to the U-M surface due to the uniform micro-pillars. However, it has great difference for the R-SML and R-SM surfaces with non-uniform micro-pillars.

Fig. 6(b) shows the schematic diagram of the replenished liquid on the R-SM surface. For the capillary pressure P_c, it is necessary to perform a weighted average of each non-uniform unit by the area occupied by different micro-pillars. Table 4 shows the surface area enhancement ratio α and capillary pressure P_c under the saturated and subcooled pool boiling. As the diameter of the micro-pillars decreases, the capillary pressure P_c and the viscous resistance P_v increase. For the surfaces with non-uniform micro-pillars, the capillary pressure P_c decreases obviously. It can be seen from Table 4 that both surface area enhancement ratio α and capillary pressure P_c have the same trend. As shown in Fig. 7, surface area enhancement ratio α and capillary pressure P_c have strong linear correlation by fitting the data points. And the goodness of fit R^2 of the two fitting curves are both 0.9997. It can be considered that the capillary pressure P_c and surface area enhancement ratio α are linearly related for the surfaces with micro-pillars in this study, and the capillary pressure P_c can be reflected by the surface area enhancement ratio α. However, there is a larger bubble separation diameter during the saturated boiling than that of the subcooled pool boiling, which leads to bubbles merging easily. And the vapor film formed on the heated surface prevents the liquid replenishment and suppresses the CHF in the previous research [6]. As a result, the CHF of the surfaces with uniform and non-uniform micro-pillars has no obvious difference under the saturated boiling as shown in Fig. 3(a) and (b), and there is no obvious relationship between the CHF and α. For subcooled pool boiling, it shows good liquid replenishment ability for the non-uniform surfaces due to small separation diameter of bubbles.

For the viscous resistance P_v, the non-uniform micro-pillars has some difference with the uniform micro-pillars. As shown in Fig. 6 (b), a non-uniform micro-pillar unit of the R-SM surface is further divided into several micro-pillar units by the red dashed lines, including a micro-pillar and its surrounding gaps. The side length of each micro-pillar unit is x_{MM} or x_{SS}. As illustrated above, the replenished liquid flow is still divided into the flow along an infinite plate and around an infinite pillar. And the pressure drop per unit length ΔP_1 caused by the flow along an infinite plate can be calculated by Eq. (24). Although the pressure drop per unit length ΔP_2

Table 4
Surface area enhancement ratio and capillary pressure drop of the different micro-pillars surfaces.

Sample	α	ΔP_c (Pa)	
		Saturated ($\Delta T_{sub} = 0$ K)	Subcooled ($\Delta T_{sub} = 25$ K))
U–S	4.73	308.82	392.48
U-M	2.88	154.41	196.24
U-L	1.94	77.21	98.12
R-SML	3.41	197.64	251.18
R-SM	3.87	240.19	305.26

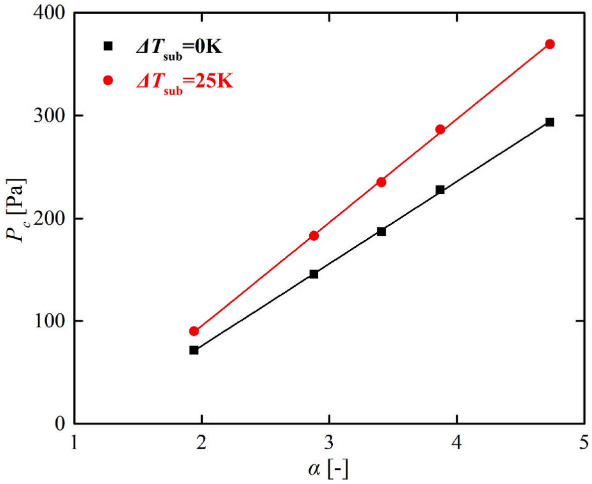

Fig. 7. Comparison of the α and ΔP_c at different boiling conditions.

caused by the flow around an infinite pillar is also calculated by Eq. (26), the flow channels will be separated to some extent due to the non-uniform micro-pillars.

The dashed lines in Fig. 6(b) is the centerline of the flow channel around the pillars. It can be seen that the dashed lines in the non-uniform region are staggered, while the red dashed lines in the uniform region is in the same line. There is a relationship of $L_M = x_{MM}$ when the flow channel is in the same line. However, L_M is larger than the side length of each micro-pillar x_{MM} because the flow channels are staggered on the non-uniform surface. Thereby the pressure drop gradient of the flow around an infinite pillar ΔP_2 decreases with the increase of the L_M, which can be expressed as:

$$\Delta P_2 = \frac{8}{9}\mathrm{Re}_D \frac{f_D \mu u_l'}{2x_{MM}^2} \tag{30}$$

The non-uniform micro-pillars can decrease the pressure drop gradient of the flow around an infinite pillar. So Eq. (28) can be further rewritten as:

$$u_l' = \frac{P_c}{w r_v} \tag{31}$$

$$w = \frac{\Delta P_1 + \Delta P_2}{u_l'} \tag{32}$$

The effective coefficient w is independent of theoretical replenished liquid velocity u_l' while ΔP_1 and ΔP_2 are proportional to the first power of u_l'. So two conclusions can be obtained from Eqs. 31 and 32:

(1) The capillary pressure P_c increases with the surface area enhancement ratio α increasing. When the effective coefficient w and vapor column r_v are fixed, the heat flux q will increase with the increase of the replenished liquid velocity u_l'. In a word, a larger surface area enhancement ratio α increases the capillary pressure P_c, thereby increasing the replenished liquid velocity u_l' and CHF.
(2) The effective coefficient w decreases with the ΔP_2 decreasing. So the replenished liquid velocity u_l' and heat flux q increase when capillary pressure P_c and vapor column r_v remain unchanged. The decreasing of viscous resistance P_v caused by the non-uniform micro-pillars improves the replenished liquid velocity u_l' and leads to the increase of the CHF. Therefore, it can be seen that the non-uniform micro-pillars can further improve the CHF, regardless of the surface area enhancement ratio α.

Some small pillars are also affected by the staggered flow channels on the R-SM surface. The non-uniform arrangement of these micro-pillars improves the rewetting effect, which the boundary has been outlined in pink in Fig. 6(b). For other micro-pillars that are not affected by the non-uniform arrangement along the flow direction on the R-SM surface, the calculation process of the ΔP_2 is the same as that of the surfaces with uniform micro-pillars. After calculating the ΔP_2 in a smallest non-uniform unit, then the total ΔP_2 on the non-uniform surfaces will be calculated by weighting average according to the area ratio of the different size pillars in the smallest non-uniform unit. And the viscous resistance P_v on the surfaces with non-uniform micro-pillars will be also obtained.

So far, the capillary pressure P_c and the viscous resistance P_v have been obtained, and the theoretical replenished liquid velocity u_l' of each chip can be calculated from Eq. (28). It is important to define the Reynolds number according to the flow velocity and characteristic length. Since the actual Reynolds number on the U-M surface can be calculated by using the actual replenished liquid velocity u_l. For U–S and U-L surfaces, the effect factors include the actual replenished liquid velocity u_l and the pillar diameter D. Although actual replenished liquid velocity u_l has little difference for the surfaces with different micro-pillars, there is a huge difference for the diameter of different pillars. So it can be considered that the pillar diameter D is the main factor affecting the Reynolds number, and the Reynolds number of surfaces with different micro-pillars can be calculated as follow:

$$\begin{aligned} &\mathrm{Re}_{U-S,sat} = 0.5 \times \mathrm{Re}_{U-M,sat} = 0.359; \mathrm{Re}_{U-L,sat} = 2 \times \mathrm{Re}_{U-M,sat} = 1.436 \\ &\mathrm{Re}_{U-S,sub} = 0.5 \times \mathrm{Re}_{U-M,sub} = 0.549; \mathrm{Re}_{U-L,sub} = 2 \times \mathrm{Re}_{U-M,sub} = 2.194 \end{aligned} \tag{33}$$

In order to facilitate CHF prediction model, the Reynolds number can be further generalized: $\mathrm{Re}_L = \mathrm{Re}_{U\text{-}L}$, $\mathrm{Re}_M = \mathrm{Re}_{U\text{-}M}$, $\mathrm{Re}_S = \mathrm{Re}_{U\text{-}S}$. Then, the Reynolds number of different non-uniform micro-pillars on the surfaces can be calculated according to **Eq. (33)**.

The correction velocity u_l'' can be obtained by using the correction factor k to correct the theoretical replenished liquid velocity u_l' of each surface:

$$u_l' = ku_l' \tag{34}$$

As can been seen from the above analysis, **Eqs. 12 and 13** are used to calculate the vapor speed u_v and spacing of vapor column λ_b, which are given as follow equations:

$$u_v = \sqrt{\frac{\sigma}{\rho_v r_v}} \tag{35}$$

$$\lambda_b = 2r_v\sqrt{\frac{\rho_v u_v + \rho_l u_l''}{\rho_l u_l''}} \tag{36}$$

So, the new CHF prediction model can be expressed as:

$$q_{CHF,pre} = \frac{\rho_v u_v \cdot 4r_v^2 h_{lv}}{\lambda_b^2} \tag{37}$$

4. Results and discussion

The CHF of surfaces with micro-pillars in this study was predicted using the previous theoretical model, which the predicted results are shown in Fig. 8 and **Table 5**. Among them, Zuber's model [20], Kandlikar's model [22] and Quan's model [23] can only be used to predict the saturated pool boiling, and they have not considered the influence of the liquid subcooling. Therefore, these three models underestimate the experimental data points under the subcooled pool boiling (ΔT_{sub} = 25 K). However, Cao et al. [8] developed a model to predict CHF under the saturated and subcooled pool boiling. It can be found that the this model does not show good applicability especially for the subcooled pool boiling. In contrast, Cao et al. [8] can predict the CHF better at saturated boiling than other three models.

The CHF predicted values of different surfaces are obtained under the saturated and subcooled pool boiling (ΔT_{sub} = 25 K) according to the new established CHF prediction model. **Fig. 9** compares the predicted CHF values calculated by the present model with the experimental values. It's worth noting that the predicted CHF values of the U-M surface is equal to the experimental values due to using the experimental data of the U-M surface to determine the correction factor k. **Fig. 9(a)** presents the predicted values under the saturated and subcooled pool boiling (ΔT_{sub} = 25 K). The predicted CHF values of two surfaces with non-uniform micro-pillars are higher than that of the surfaces with uniform micro-pillars at subcooled pool boiling (ΔT_{sub} = 25 K), which is consistent with the experimental values. At saturated boiling, the CHF prediction values of five surfaces are relatively close to the experimental values.

Compared with the CHF prediction models proposed by previous researchers in the literature [8,20,22,23], it can be seen that the new model can better predict the CHF of the micro-pillar surfaces under saturated and subcooled pool boiling. Besides, some previous experimental data of CHF on the square micro-pin-fin surfaces [1] were collected to verify the accuracy of this new CHF prediction

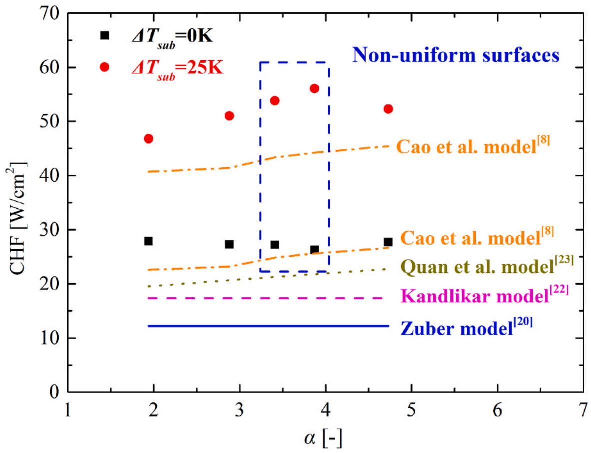

Fig. 8. Comparison between the experimental and the prediction results of CHF model in **Refs.** [8,20,22,23].

Table 5
MAD[a] (mean absolute deviation) of four CHF prediction model.

Authors	U–S		U-M		U-L		R-SML		R-SM	
	ΔT_{sat}	ΔT_{sub}	ΔT_{sat}	ΔT_{sub}	ΔT_{sat}	ΔT_{sub}	ΔT_{sat}	ΔT_{sub}	ΔT_{sat}	ΔT_{sub}
Zuber [20]	56.3		55.6	–	56.6	–	55.5	–	54.0	–
Kandlikar [22]	37.7		36.7	–	38.1	–	36.6	–	34.3	–
Quan et al. [23]	18.4		24.3	–	30.1	–	22.0	–	17.0	–
Cao et al. [8]	4	13.1	15.3	18.9	19.2	13.2	9.2	19.3	2.4	21

[a] $MAD = \frac{1}{N}\cdot\sum\frac{\left|(CHF)_{\exp}-(CHF)_{pre}\right|}{(CHF)_{\exp}}\cdot 100$

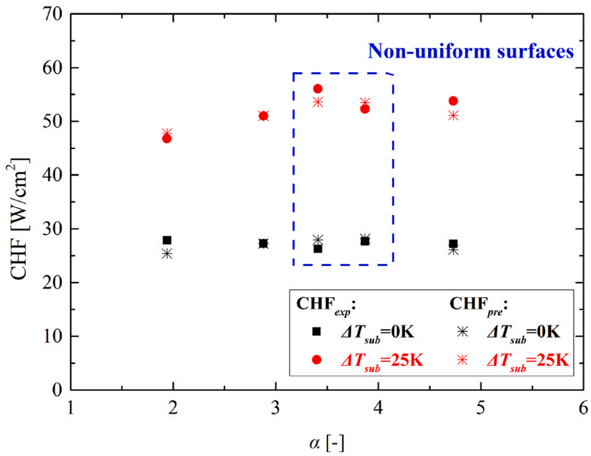

(a)

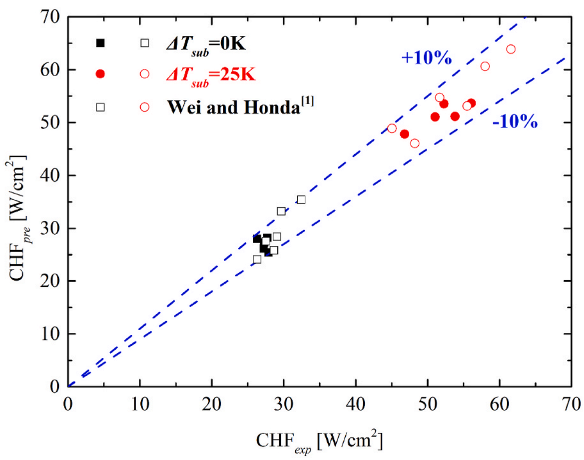

(b)

Fig. 9. Comparison of the CHF prediction values by the new model and experimental data.

model. As shown in Fig. 9(b), we can see that the new model can predict previous data within ± 10% error band, which further confirms the rationality of the new model.

The establishment of new model is helpful to understand the poo boiling mechanism of the replenished liquid on the surfaces with uniform and non-uniform micro-pillars and its effect on the increasing of CHF. As introduced above, on the one hand, the non-uniform arrangement is beneficial to reduce the viscous resistance P_v and increases the replenished liquid velocity u_l. On the other hand, the surface area enhancement ratio α increases the capillary pressure P_c, thereby increasing the replenished liquid velocity u_l.

The replenished liquid velocity u_l can be approximately used to reflect the wickability of different surfaces with micro-pillars under different experimental conditions. So, for the surfaces discussed in this paper, it can be considered that both the surface area enhancement ratio α and the non-uniform arrangement increase the surface wickability (replenished liquid velocity u_l). As a result, the CHF can be further improved.

5. Conclusions

In this study, a CHF prediction model for the surfaces with uniform and non-uniform micro-pillars was proposed based on the replenished liquid effect. The model considered the influence of non-uniformity on the micro-pillar surfaces, which combined the vapor velocity u_v with the spacing and radius of vapor column (λ_b and r_v). This new CHF model shows good prediction ability for the surfaces with uniform and non-uniform micro-pillars under saturated and subcooled pool boiling. The main conclusions can be obtained as follows:

(1) The new model in this paper estimated the impact of the non-uniform micro-pillars, and the prediction deviation for the five micro-pillar surfaces can basically be controlled within 10%.
(2) Analyzing the mechanism of replenished liquid, it is found that the surface area enhancement ratio α can increase the capillary pressure P_c by enhancing the wickability. And the non-uniform micro-pillars array reduces the viscous resistance P_v.
(3) The replenished liquid velocity u_l can reflect the wickability effect on the surfaces with micro-pillars. The surface area enhancement ratio α and non-uniform micro-pillars array increase the surface wickability, which further improve the CHF.

Author statement

Yonghai Zhang: Conceptualization, Methodology, Writing - review & editing, Supervision, Resources.
Xiang Ma: Writing - original draft, Software, Investigation.
Zhiqiang Zhu: Formal analysis, Data curation, Supervision.
Lian Duan: Validation, Methodology.
Jinjia Wei: Conceptualization, Resources.

Declaration of competing interest

The authors declare that they have no known competing financial interests or personal relationships that could have appeared to influence the work reported in this paper.

Acknowledgements

This work is supported by the Basic Research Project of Shenzhen Knowledge Innovation Program (No.JCYJ20180306170627132), National Natural Science Foundation of China (No.51976163, 51636006, 51961135102, U1738119), Young Elite Scientists Sponsorship Program by CAST (No.2018QNRC001), ESA-CMSA Joint Boiling Project (TGMTYY00-RW-05-1.00), and Shanxi Creative Talents Promotion Plan-Technological Innovation Team (2019TD-039).

References

[1] J.J. Wei, H. Honda, Effects of fin geometry on boiling heat transfer from silicon chips with micro-pin-fins immersed in FC-72, Int. J. Heat Mass Tran. 46 (21) (2003) 4059–4070.
[2] B. Xun, K. Li, P.G. Chen, W.-R. Hu, Effect of interfacial heat transfer on the onset of oscillatory convection in liquid bridge, Int. J. Heat Mass Tran. 52 (19–20) (2009) 4211–4220.
[3] B. Xun, K. Li, W.-R. Hu, N. Imaishi, Effect of interfacial heat exchange on thermocapillary flow in a cylindrical liquid bridge in microgravity, Int. J. Heat Mass Tran. 54 (9–10) (2011) 1698–1705.
[4] H.S. Ahn, G. Park, J.M. Kim, J. Kim, M.H. Kim, The effect of water absorption on critical heat flux enhancement during pool boiling, Exp. Therm. Fluid Sci. 42 (2012) 187–195.
[5] L.N. Dong, X.J. Quan, P. Cheng, An experimental investigation of enhanced pool boiling heat transfer from surfaces with micro/nano-structures, Int. J. Heat Mass Tran. 71 (2014) 189–196.
[6] L. Duan, B. Liu, B.J. Qi, Y.H. Zhang, J.J. Wei, Pool boiling heat transfer on silicon chips with non-uniform micro-pillars, Int. J. Heat Mass Tran. 151 (2020) 119456.
[7] Z.Y. Lei, B. Liu, P.Z. Xu, Y.H. Zhang, J.J. Wei, The pool boiling heat transfer and critical vapor column coalescence mechanism of block-divided microstructured surfaces, Int. J. Heat Mass Tran. 150 (2020) 119362.
[8] Z. Cao, B. Liu, C. Preger, Z. Wu, Y.H. Zhang, X.L. Wang, M.E. Messing, K. Deppert, J.J. Wei, B. Sundén, Pool boiling heat transfer of FC-72 on pin-fin silicon surfaces with nanoparticle deposition, Int. J. Heat Mass Tran. 126 (2018) 1019–1033.
[9] C.-K. Guan, J.F. Klausner, R. Mei, A new mechanistic model for pool boiling CHF on horizontal surfaces, Int. J. Heat Mass Tran. 54 (17–18) (2011) 3960–3969.
[10] H. Jo, D.I. Yu, H. Noh, H.S. Park, M.H. Kim, Boiling on spatially controlled heterogeneous surfaces: wettability patterns on microstructures, Appl. Phys. Lett. 106 (18) (2015) 181602.
[11] S.H. Kim, G.C. Lee, J.Y. Kang, H.S. Park, M.H. Kim, A study of nucleate bubble growth on microstructured surface through high speed and infrared visualization, Int. J. Multiphas. Flow 95 (2017) 12–21.
[12] B. Liu, J. Liu, Y.H. Zhang, J.J. Wei, W.J. Wang, Experimental and theoretical study of pool boiling heat transfer and its CHF mechanism on femtosecond laser processed surfaces, Int. J. Heat Mass Tran. 132 (2019) 259–270.
[13] B. Liu, J. Liu, J. Zhou, B. Yuan, Y.H. Zhang, J.J. Wei, W.J. Wang, Experimental study of subcooled boiling pool heat transfer and its “hook back” phenomenon on micro/nanostructured surfaces, Int. Commun. Heat Mass Tran. 100 (2019) 73–82.
[14] Y.H. Zhang, J. Zhou, W.J. Zhou, B.J. Qi, J.J. Wei, CHF correlation of boiling in FC-72 with micro-pin-fins for electronics cooling, Appl. Therm. Eng. 138 (2018) 494–500.
[15] X. Kong, Y.H. Zhang, J.J. Wei, Experimental study of pool boiling heat transfer on novel bistructured surfaces based on micro-pin-finned structure, Exp. Therm. Fluid Sci. 91 (2018) 9–19.
[16] J. Zhou, B.J. Qi, J.J. Wei, Critical heat flux on heterogeneous fractal surfaces with micro-pin-fins in pool boiling Part I: the effects of distribution and subcooling, Int. J. Heat Mass Tran. 136 (2019) 1338–1348.
[17] J. Zhou, B.J. Qi, J.J. Wei, Critical heat flux on heterogeneous fractal surfaces with micro-pin-fins in pool boiling – Part II: model establishment and analysis, Int. J. Heat Mass Tran. 136 (2019) 46–54.
[18] M.M. Rahman, E. Olceroglu, M. McCarthy, Role of wickability on the critical heat flux of structured superhydrophilic surfaces, Langmuir 30 (37) (2014) 11225–11234.

[19] K.-H. Chu, R. Enright, E.N. Wang, Structured surfaces for enhanced pool boiling heat transfer, Appl. Phys. Lett. 100 (24) (2012) 241603.
[20] N. Zuber, On the instabilityof boiling heat transfer, Trans. ASME 80 (1958) 711–720.
[21] S.G. Liter, M. Kaviany, Pool-boiling CHF enhancement by modulated porous-layer coating: theory and experiment, Int. J. Heat Mass Tran. 44 (22) (2001) 4287–4311.
[22] S.G. Kandlikar, A theoretical model to predict pool boiling CHF incorporating effects of contact angle and orientation, J. Heat Tran. 123 (6) (2001) 1071–1079.
[23] X.J. Quan, L.N. Dong, P. Cheng, A CHF model for saturated pool boiling on a heated surface with micro/nano-scale structures, Int. J. Heat Mass Tran. 76 (2014) 452–458.
[24] N.S. Dhillon, J. Buongiorno, K.K. Varanasi, Critical heat flux maxima during boiling crisis on textured surfaces, Nat. Commun. 6 (2015) 8247.
[25] Z. Wu, Z. Cao, B. Sundén, Saturated pool boiling heat transfer of acetone and HFE-7200 on modified surfaces by electrophoretic and electrochemical deposition, Appl. Energy 249 (2019) 286–299.
[26] Y.M. Chen, F. Mayinger, Measurement of heat transfer at the phase interface of condensing bubbles, Int. J. Multiphas. Flow 18 (6) (1992) 877–890.
[27] T. Young, An essay on the cohesion of fluids, Phil. Trans. Roy. Soc. Lond. 95 (1805) 65–87.
[28] B.R. Munson, D.F. Young, T. Okiishi, W.W. Huebsch, Fundamentals of Fluid Mechanics, Sixth Edition, Differential Analysis of Fluid Flow, Ch. 6, 2009, pp. 307–308.

Nomenclature

A_b: Unit area, cm^2
A_v: Vapor column area, cm^2
c_p: Specific heat, kJ/(kg·K)
D: Pillar diameter, m
ΔE: Energy change, J
f: Resistance factor
F_D: Resistance, N
Fo: Fourier number
g: Gravitational acceleration, m/s^2
h_{lv}: Latent heat of vaporization, J/kg
h_o: Micro-pillars height/Liquid thickness, m
k: Correction factor
K_v: Permeability of the surface, m^2
L/x: Length, m
Ja: Jakob number, $\rho_l c_{pl}(T_{sat}\text{-}T_b)/\rho_g h_{lv}$
ΔP: Pressure drop, kPa
ΔP_c: Capillary pressure drop, Pa
ΔP_v: Viscous resistance pressure drop, Pa
Pr: Prandtl number
q_{CHF}: Heat flux, W/cm^2
r_M: Micro-pillar radius, mm
r_v: Vapor column radius, mm
R^2: Goodness of fit
Re: Reynolds number
S: Pillar facing flow area, cm^2
t: Moment, s
T: Temperature, K
T_b: Temperature of bulk liquid, K
ΔT_{sat}: Superheat temperature, K
ΔT_{sub}: Subcooled temperature, K
u: Velocity, m/s
u_l: Actual replenished liquid velocity, m/s
u_l': Theoretical replenished liquid velocity, m/s
u_l'': Correction velocity, m/s
u_v: Vapor column velocity, m/s
ΔV: Unit volume, L
w: Effective coefficient

Greek symbols

α: Surface area enhancement ratio
β: Ratio of bubble radius
λ: Instability wavelength, mm
λ_b: Spacing of vapor column, mm
v: Kinematic viscosity, m^2/s
μ: Dynamic viscous, Pa·s
θ: Contact angle, $^\circ$
σ_{lv}: Liquid-vapor interface surface tension, N/m
σ_{sl}: Solid-liquid surface tension, N/m
σ_{sv}: Solid-vapor surface tension, N/m
ρ: Density, kg /m^3

Subscripts

c: Critical
KH: Kelvin-Helmholtz
l: Liquid phase
pre: Prediction
RT: Rayleigh-Taylor
sat: Saturated
sub: Subcooled
v: Vapor phase